

A unique ultrarefractory inclusion from the Murchison meteorite

STEVEN B. SIMON¹* ANDREW M. DAVIS² AND LAWRENCE GROSSMAN^{1,2}

¹Department of the Geophysical Sciences, University of Chicago, 5734 South Ellis Avenue, Chicago, Illinois 60637, USA

²Enrico Fermi Institute, University of Chicago, 5640 South Ellis Avenue, Chicago, Illinois 60637, USA

*Correspondence author's e-mail address: sbs8@midway.uchicago.edu

(Received 1995 May 8; accepted in revised form 1995 October 23)

Abstract—Through freeze-thaw disaggregation of the Murchison meteorite, we have recovered a refractory inclusion, HIB-11, that is unique in terms of its texture, mineral compositions, and bulk composition. It consists of anhedral, Y-rich (1.6 wt% Y_2O_3) perovskite and lathlike spinel grains enclosed in a matrix of fine-grained, Sc-rich (10.5 wt% Sc_2O_3 avg.), Ti-rich (12.6 wt% TiO_2 avg., reporting all Ti as TiO_2) clinopyroxene. The chondrite-normalized rare earth element (REE) pattern is complex, with light REE (LREE) at $\sim 10\times$ C1, abundances increasing from Gd through Ho (the latter at $\sim 10^4\times$ C1), decreasing through Yb at $200\times$ C1, and Lu at $\sim 400\times$ C1. The pattern reflects several stages of high-temperature volatility fractionation. Removal of Lu and Er from the source gas in the first condensation event was followed by partial to complete removal of the somewhat less refractory heavy REE, Gd through Ho, in the HIB-11 precursors by condensation from the fractionated residual gas in a second event. Both of these events probably reflect condensation of REE into ZrO_2 or a mixed Zr-, Sc-, Ti-, Y-oxide at temperatures too high for hibonite stability. A second, lower-temperature component, which was subsequently added, had fractionated (Nd-poor, Ce-rich) LREE abundances that resulted from condensation from a gas that had undergone prior removal of the more refractory LREE, resulting in enrichment in Ce and the most volatile REE, Eu and Yb. The aggregate was then melted and quickly cooled, forming a fine-grained spherule. This is the first reported inclusion in which the two most refractory REE, Lu and Er, are strongly fractionated from the other REE. An absence of mass fractionation among the Ti isotopes indicates that HIB-11 is not an evaporative residue, implying that volatility fractionation of trace elements took place during condensation. The fact that the two most refractory heavy REE could be separated from the other, only slightly less refractory heavy REE suggests that a wide variety of REE patterns is possible, and that ultrarefractory inclusions with other unusual REE patterns, important recorders of nebular condensation, may yet be discovered.

INTRODUCTION

It is not unusual for Ca-, Al-rich inclusions (CAIs) from carbonaceous chondrites to have chondrite-normalized rare earth element (REE) abundance patterns that exhibit volatility-dependent fractionation rather than smooth variations as a function of ionic radius. A common type of such a pattern, defined as Group II (Mason and Martin, 1977), is characterized by relatively high, flat light REE (LREE) abundances, progressively decreasing heavy REE (HREE) abundances from Gd through Lu, negative Eu and Yb anomalies relative to LREE, and positive Tm anomalies (relative to adjacent HREE). Group II inclusions probably contain material that condensed from a gas from which the most refractory REE (Lu, Er, Ho, and Dy) had been removed by prior condensation (Boynton, 1975; Davis and Grossman, 1979). Although $\sim 20\%$ of all CAIs have Group II patterns (Davis, 1991), inclusions with complementary, ultrarefractory-element-enriched patterns are rare. Only six have been reported (Noonan *et al.*, 1977; Palme *et al.*, 1982; Ekambaram *et al.*, 1984a,b; Davis, 1984, 1991), and petrographic data are available for only four of these. Noonan *et al.* (1977) and Davis (1991) described an Ornans inclusion, 1105, that consists of a Ti-, Sc-, Zr-, Y-oxide, enriched in the most refractory REE, enclosed in a silicate glass that contains TiO_2 , Sc_2O_3 , Y_2O_3 , and ZrO_2 . The silicate glass is, in turn, enclosed in an amoeboid olivine inclusion. Another inclusion from Ornans, RNZ, was found as a result of a search for Ir-rich phases (Palme *et al.*, 1982). Part of it was lost during thin section preparation (after irradiation); the remaining part consists of Ir-rich NiFe and Os-, Ru-rich metal nuggets. OSCAR, also from Ornans (Davis, 1984), consists of Y-rich perovskite, spinel, and hibonite enclosed in Sc-rich fassaite.

Mighei 3483-1-1 is an aggregate of spinel balls with abundant Y-rich perovskite and minor amounts of hibonite and ZrO_2 (Davis, 1991). These inclusions have light REE abundances of ~ 30 – $60\times$ C1, negative Eu anomalies, increasing heavy REE abundances with atomic number from Gd ($\sim 10^3\times$ C1) through Er ($10^4\times$ C1), negative Yb anomalies, and Lu at $\sim 10^4\times$ C1 (Palme *et al.*, 1982; Noonan *et al.*, 1977; Davis, 1991). Two other inclusions have some ultrarefractory affinities. Boynton *et al.* (1980) reported an inclusion with a grossly similar pattern (*i.e.*, negative Eu and Yb anomalies, high heavy REE abundances including Lu), but the abundances of all the REE are $<100\times$ C1 and the heavy REE, except for Tm and Yb, are equally enriched rather than increasingly enriched from Gd through Er. Fahey *et al.* (1994) recently described a hibonite-, hercynite-rich inclusion from Lancé in which hibonite and perovskite are enriched in HREE relative to LREE. They interpreted this feature as indicative of an ultrarefractory component, although the Tb/La ratio in the Lancé inclusion is only ~ 2 , not ~ 1000 as in true ultrarefractory inclusions.

We report here an ultrarefractory inclusion from Murchison (CM2) that is unique petrographically and chemically. It consists of spinel and Y-rich perovskite enclosed in Sc-fassaite in a texture different from that of OSCAR, and, unlike in other ultrarefractory inclusions, Ho is the REE with the greatest enrichment factor relative to C1 chondrites. This inclusion is, thus, very important because it provides us with a previously unsampled record of chemical processes that occurred in a very early, high-temperature stage of solar nebular evolution about which we could otherwise only speculate. Neither the conditions under which the REE fractionated nor the inclusion's highly refractory bulk composition

have been investigated experimentally. Such an inclusion provides the most direct means of studying gas/solid fractionation in the early solar nebula, a fundamental process in the formation of the Solar System. Preliminary results of this study were given by Simon *et al.* (1993).

ANALYTICAL METHODS

The sample, HIB-11, was recovered by hand-picking from the high-density ($\rho > 3.5$) separate obtained from the products of freeze-thaw disaggregation of Murchison by the method of MacPherson *et al.* (1980). A polished thin section of HIB-11 was examined with a JEOL JSM-35 scanning electron microscope equipped with a Kevex energy-dispersive x-ray system. Quantitative wavelength-dispersive mineral analyses were performed with a fully automated Cameca SX-50 electron microprobe operated at 15 kV with a beam current of 40 nA. Synthetic glass and crystal (MgAl_2O_4 , thortveitite, and oxides) and natural mineral (andradite) standards were used. Counting times were either 30 s (Mg, Al, Si, Fe), 40 s (Ca, Ti), 50 s (Sc, Y), or 60 s (Cr, Y, Zr). Data were reduced via the modified ZAF correction procedure PAP (Pouchou and Pichoir, 1984). In addition, electron probe analyses of pyroxene were corrected for interference between a second-order ScK_{α} peak and the first-order ZrL_{α} peak used for Zr analysis. We were, however, able to resolve the TiK_{β} and VK_{α} peaks by analyzing for these elements with an LIF crystal and setting the background measurement positions appropriately.

Trace element and isotopic analyses were obtained using the University of Chicago AEI IM-20 ion microprobe. The analytical techniques used are similar to those described in Hinton *et al.* (1988), Davis *et al.* (1991), Simon *et al.* (1991), and MacPherson and Davis (1993, 1994).

RESULTS

Petrography

Inspection with the binocular microscope prior to sectioning showed the sample to be a pale blue, frosted spherule $\sim 120 \mu\text{m}$ in diameter. Figure 1 is a backscattered electron image (BEI) of the thin section. It shows that the sample consists of anhedral perovskite grains, up to $10 \mu\text{m}$ across, and anhedral spinel in a matrix of pyroxene, which is seen to be fine-grained when viewed in transmitted light. There is one relatively large cavity and many small void spaces throughout, reminiscent of the porosity observed in the blue, hibonite plus spinel spherules from Murchison (*e.g.*, Macdougall, 1981; MacPherson *et al.*, 1983). In the present case, the voids occur predominantly in pyroxene, but there are also some in spinel. The pyroxene is somewhat less porous in the interior of the inclusion than at the rim. The spinel has an unusual, lathlike habit, and the laths are up to $\sim 15 \mu\text{m}$ long. Spinel like this has been reported in an inclusion from Mighei (MacPherson and Davis, 1994) and in only two other inclusions from Murchison, both of which are spinel-hibonite aggregates described by MacPherson *et al.* (1984), in which spinel appears to have pseudomorphically replaced hibonite and in which the two phases are not intergrown. In HIB-11, spinel and pyroxene are finely intergrown, as shown in Fig. 1b, and hibonite is absent. A grid count of 1541 points on the BEI gives a mode of 53.5 vol% pyroxene, 34.8 vol% spinel, and 11.7 vol% perovskite. OSCAR, an ultrarefractory inclusion from Ornans (Davis, 1984), also has perovskite and spinel enclosed in pyroxene and is the ultrarefractory inclusion that is the most similar to HIB-11, although their textures are different. OSCAR is a coarser-grained inclusion that consists of a band of perovskite grains with accessory ZrO_2 and refractory noble metal-rich grains and a separate region containing spinel and hibonite, all contained in a matrix of Sc-rich fassaite. In contrast, perovskite and spinel occur throughout HIB-11, rather than in specific regions, and almost every grain is completely enclosed by pyroxene.

Mineral Chemistry

Pyroxene—Representative electron probe analyses are given in columns 1 through 5 of Table 1 in order of decreasing Sc_2O_3

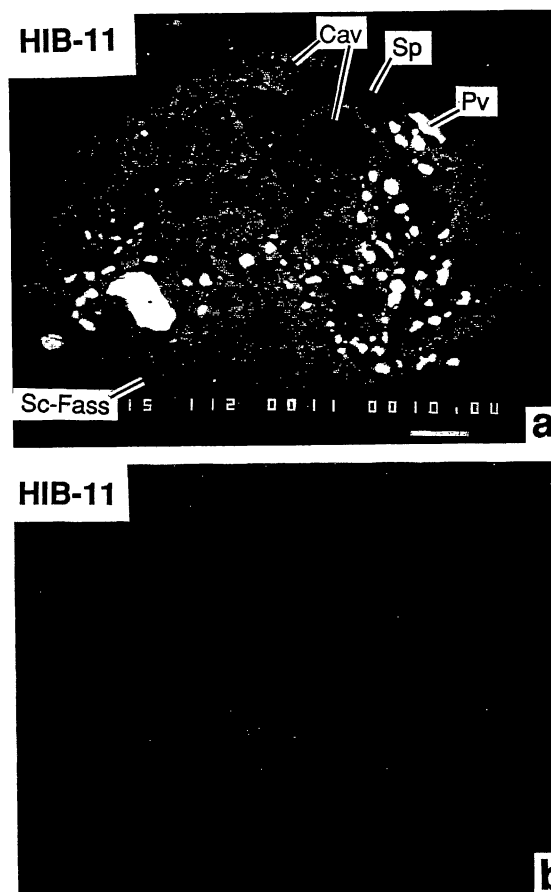


FIG. 1. Backscattered electron images of HIB-11. Both scale bars are $10 \mu\text{m}$. (a) View of the entire chip, showing perovskite (Pv) and spinel (Sp) enclosed in Sc-rich fassaite (Sc-Fass), with many cavities (Cav). Note the lath-shaped spinel grains. (b) Close-up view, showing spinel laths (dark gray) enclosed in Sc-fassaite (light gray). Void spaces are black.

abundance. Analyses of fassaite from an Allende Type B1 CAI and from OSCAR are also shown for comparison. The pyroxene in HIB-11 is Sc-, Ti-, Al-rich, and Mg-poor relative to that in Type B refractory inclusions. With 5.7 wt%–15 wt% Sc_2O_3 and an average of 10.5 wt%, the pyroxene in HIB-11 has Sc_2O_3 contents between those of fassaite in Type B CAIs, which range from ppm-level to ~ 1 wt% (Simon *et al.*, 1991), and those of fassaite in OSCAR, which range from 11.4 wt% to 18.3 wt% (Davis, 1984) and average 15 wt%. A similar relationship holds for ZrO_2 , which is <0.2 wt% in fassaite from Type Bs (Simon *et al.*, 1991), ranges from 0.16 to 1.1 and averages 0.64 wt% in HIB-11 pyroxene, and ranges from 1.3 to 6.7 and averages 3.3 wt% in OSCAR fassaite. In HIB-11 pyroxene, $\text{TiO}_2^{\text{tot}}$ (all Ti calculated as TiO_2) contents (10.5 wt%–14.1 wt%) are at the high end of the range for Type B fassaite (Simon *et al.*, 1991) and are higher than those of OSCAR fassaite (Davis, 1984). The $\text{Ti}^{3+}/\text{Ti}^{\text{tot}}$ ratios in HIB-11 fassaite range from 0.2 to 0.6, which is between those of fassaite in Type B CAIs (generally 0.5–0.8) and in OSCAR (0.1–0.4). Relationships between oxides are illustrated in Fig. 2. Several analyses, shown in open symbols, have lower Sc_2O_3 and ZrO_2 and higher MgO and SiO_2 contents than the other analyses. These spots are not restricted to any specific area of the inclusion. As in fassaite from Type B inclusions (Simon *et al.*, 1991), MgO and SiO_2 are positively correlated with each other and

TABLE 1. Electron probe analyses of fassaite.

	1	2	3	4	5	6	7
MgO	1.06	1.23	1.10	2.92	5.00	10.99	1.64
Al ₂ O ₃	25.52	26.33	26.61	26.73	22.51	15.63	26.07
SiO ₂	21.13	21.45	21.52	23.00	29.11	42.43	22.42
CaO	23.72	23.63	23.83	23.01	23.65	25.16	23.19
Sc ₂ O ₃	14.57	13.63	12.77	9.89	5.67	0.08	14.97
TiO ₂ ^{tot}	12.62	11.49	13.31	13.36	11.24	6.78	6.66
V ₂ O ₃	0.54	0.67	0.62	0.63	0.86	0.18	0.98
Cr ₂ O ₃	0.07	0.09	0.07	0.08	0.16	0.06*	n.a.
FeO	BLD	BLD	BLD	BLD	BLD	0.01	0.56
Y ₂ O ₃	0.24	0.30	0.27	0.34	0.26	0.01*	0.52
ZrO ₂	0.85	0.93	0.87	0.68	0.20	0.05*	3.26
Ti ₂ O ₃	5.05	4.11	5.75	3.42	5.24	4.30	1.59
TiO ₂	7.09	6.97	6.97	9.25	5.36	1.95	4.90
TOTAL	99.84	99.34	100.38	99.95	98.02	100.73	100.10
Si	0.836	0.849	0.843	0.881	1.129	1.542	0.877
Al	1.164	1.151	1.157	1.119	0.871	0.458	1.123
Al	0.027	0.077	0.072	0.087	0.159	0.211	0.085
Mg	0.063	0.072	0.064	0.166	0.289	0.596	0.095
Fe	0	0	0	0	0	0	0.018
Sc	0.502	0.470	0.436	0.330	0.192	0.002	0.513
V	0.014	0.018	0.016	0.016	0.022	0.005	0.029
Cr	0.002	0.003	0.002	0.003	0.005	0	—
Ti ³⁺	0.166	0.135	0.188	0.112	0.171	0.132	0.052
Ti ⁴⁺	0.210	0.207	0.205	0.273	0.157	0.054	0.145
Zr	0.016	0.018	0.017	0.013	0.004	0	0.063
Ca	0.995	0.994	0.994	0.993	0.995	1.000	0.986
Y	0.005	0.006	0.006	0.007	0.005	0	0.014**

1–5: HIB-11; 6: Allende Type B1 CAI TS34 (Simon *et al.*, 1991);

7: OSCAR (A. M. Davis, unpub. data) by ion probe.

* by ion probe.

** Y + REE cations.

n.a. = not analyzed.

BLD = Below limit of detection of 0.05 wt% FeO.

TiO₂^{tot} = All Ti as TiO₂ (not included in oxide sum). Analyses are normalized to four total cations, including exactly one M2 cation (Ca and Y) and two tetrahedral cations (Si and Al) per six oxygens. The methods of Beckett (1986) were used to calculate Ti³⁺ contents.

negatively correlated with Sc₂O₃, the latter oxide being more strongly compatible in fassaite than MgO during fractional crystallization from CaO-, Al₂O₃-rich silicate melts. Zirconium oxide is compatible in Type B fassaite (Simon *et al.*, 1991), and that appears to be the case here as well, as shown by the positive correlation between ZrO₂ and Sc₂O₃ (Fig. 2c). Although Y is incompatible in fassaite (Simon *et al.*, 1991), there is no overall negative correlation on a plot of Y₂O₃ vs. Sc₂O₃ (Fig. 2d), because the range of Y₂O₃ contents in the several analyses with relatively low Sc₂O₃ contents overlaps that of the analyses with higher Sc₂O₃ contents. Among the latter, however, there is an anticorrelation between Y₂O₃ and Sc₂O₃.

Spinel—Spinel is nearly pure MgAl₂O₄, with ~0.3 wt% Cr₂O₃ and ~0.5 wt% V₂O₃ (Table 2). For the latter, this is at the high end of the range for Type B CAIs and lower than the V₂O₃ content of OSCAR spinel (0.8 wt%) (Davis, unpub. data). The V₂O₃ content of HIB-11 spinel is also lower than that of spinel in Allende fluffy Type A inclusions (MacPherson and Grossman, 1984). The TiO₂ contents are relatively high, ranging from 0.7 wt% to 1.5 wt%. They are not correlated with SiO₂ but may reflect some contamina-

TABLE 2. Electron probe analyses of spinel and perovskite (wt%).

	Sp	Sp	Pv
MgO	27.94	27.95	0.02
Al ₂ O ₃	69.18	69.03	0.84
SiO ₂	0.17	0.16	0.08
CaO	0.25	0.39	38.63
Sc ₂ O ₃	n.a.	n.a.	0.56
TiO ₂	0.67	0.68	55.97
V ₂ O ₃	0.49	0.46	0.40
Cr ₂ O ₃	0.27	0.29	n.a.
FeO	0.07	0.02	BLD
Y ₂ O ₃	n.a.	n.a.	1.60
ZrO ₂	n.a.	n.a.	0.21
TOTAL	99.04	98.98	98.31
Mg	1.000	1.001	0.001
Al	1.959	1.956	0.023
Si	0.004	0.004	0.002
Ca	0.006	0.010	0.956
Sc	—	—	0.011
Ti	0.012	0.012	0.972
V	0.010	0.009	0.006
Cr	0.005	0.006	—
Fe	0.001	0	0
Y	—	—	0.020
Zr	—	—	0.002
Total Cations	2.997	2.998	1.993
No. of Ox	4	4	3

Sp = spinel. Pv = perovskite. In perovskite, Mg, Al, Si, and Ca were analyzed at 15 kV and 25 nA and the remaining elements were analyzed at 25 kV and 200 nA. n.a. = not analyzed.

BLD = Below limit of detection of 0.005 wt% FeO.

tion by perovskite. The spinel does not contain excess Al₂O₃, as has been reported for spinel in an ultrarefractory rim on a CAI (El Goresy *et al.*, 1984) and in spinel in a grossite-bearing spherule from Murchison (Simon *et al.*, 1994b).

Perovskite—Only one perovskite grain was large enough for an analysis uncontaminated by adjacent phases (Table 2). It is enriched in Y₂O₃ (1.6 wt%) and Sc₂O₃ (0.6 wt%) relative to typical CAI perovskite, but it is not as enriched as that in OSCAR, which has 5.9 wt% and 0.9 wt% Y₂O₃ and Sc₂O₃, respectively (Davis, 1984).

Major Element Bulk Composition

The major element bulk composition of HIB-11, calculated from phase compositions and their modal abundances and densities, is, by weight: 11% MgO; 38% Al₂O₃; 12% SiO₂; 17% CaO; 5.5% Sc₂O₃; 2.7% Ti₂O₃; 11% TiO₂; and 0.4% FeO. HIB-11 has about one-half the SiO₂, one-half to two-thirds the CaO, and several times the TiO₂ of typical Type A and B refractory inclusions from CV3 chondrites (see, e.g., Sylvester *et al.*, 1993). OSCAR, with higher pyroxene and perovskite and lower spinel contents than HIB-11 (Davis, 1984), has higher SiO₂, CaO, Sc₂O₃, and TiO₂, and lower MgO and Al₂O₃ contents than HIB-11. Its bulk composition, calculated the same way as for HIB-11, is: 3.4% MgO; 25% Al₂O₃; 16% SiO₂; 23% CaO; 11% Sc₂O₃; 14% TiO₂^{tot}; and 0.8% FeO, plus several wt% REE oxides and Y₂O₃.

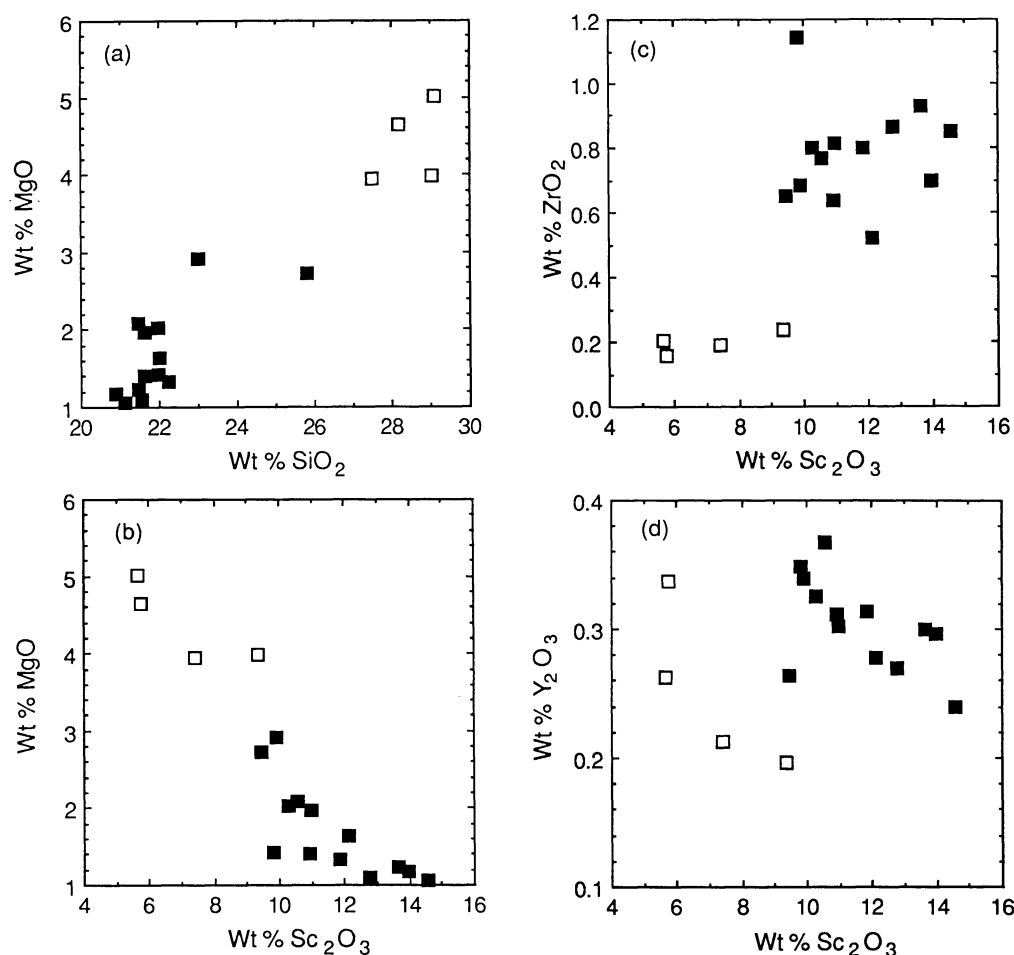


FIG. 2. Abundances of some oxides in HIB-11 fassaite. (a) MgO vs. SiO₂. The MgO contents are much lower than in fassaite from Type B CAIs. (b) MgO vs. Sc₂O₃. (c) ZrO₂ vs. Sc₂O₃. The Sc₂O₃ is anticorrelated with MgO and positively correlated with ZrO₂. (d) Y₂O₃ vs. Sc₂O₃. Open symbols represent the low-Sc₂O₃ analyses discussed in the text.

Trace Element Abundances

Eight points were analyzed by ion microprobe and representative analyses are given in Table 3. All of the analytical volumes contain fassaite and spinel \pm perovskite, and their relative proportions can be estimated from the major element abundances. Analysis #1 in Table 3 has higher MgO and Al₂O₃ than does the fassaite in HIB-11 (Table 1), indicating some contribution from spinel. The CaO and TiO₂ are not enriched, indicating that the perovskite component is negligible, so analysis #1 is probably mostly fassaite with minor spinel. In contrast, analysis #2 in Table 3 has high CaO and TiO₂ and low MgO and SiO₂ contents and, therefore, has a high perovskite component with minor amounts of spinel and fassaite. Analyses #3 and #4 sampled all three phases. They are in roughly equal proportions in #3; fassaite dominates #4.

Regardless of the proportions of phases analyzed, Sc and Y abundances in all ion probe analyses are $>1.6 \times 10^3 \times$ CI, Zr is $>300 \times$ CI, and Nb is $>100 \times$ CI. Chondrite-normalized REE abundances (Fig. 3) show strong enrichments in most of the HREE and Y relative to the LREE and a negative Yb anomaly, which is typical of ultrarefractory inclusions (e.g., Palme *et al.*, 1982; Davis, 1991). Unlike most ultrarefractory inclusions, in which Lu and Er have the greatest enrichment factors relative to C1 chondrites, in HIB-11, Ho, at $1.5 \times 10^4 \times$ C1 chondrites in analysis #2, has the greatest enrichment factor, and Dy is second highest at $8.8 \times 10^3 \times$ C1. Lutetium is depleted relative to the other refractory REE, almost to the level of the LREE (Fig. 3). In addition, in HIB-11, Y is depleted relative to Dy and Ho; whereas in other ultrarefractory

inclusions, Y has enrichment factors that are greater than those of Dy and Ho and equivalent to those of Er (e.g., Davis, 1991). Another unusual feature of the patterns is the enrichment in Ce, one of the most volatile REE, relative to the other LREE. Several analyses have chondrite-normalized Ce/La ratios of ~ 4 .

One analysis, #4 in Table 3 and Fig. 3, is quite different from the others. The HREE pattern is the same as, and HREE abundances are slightly higher than, those in the other analyses (except for the perovskite-rich spot, #2), but the LREE are a factor of 10–100 higher than in the other analyses. As shown in Table 3, this analysis is also highest in other incompatible elements, including Th (400 ppm) and U (16 ppm). For each ion microprobe analysis, six mass cycles (from 238, U, to 7, Li) were collected. For analysis #4, Th, U, Nb, and LREE varied together, all rising to a maximum and then falling gradually as the ion beam drilled deeper into the sample. For example, sequential Th contents in the six cycles were 150, 720, 550, 350, 100, and 120 ppm. These variations were accompanied by only minor variations in the proportions of MgO, Al₂O₃, SiO₂, CaO, Sc₂O₃, TiO₂, and most other trace elements. It seems likely that the ion probe beam sputtered through an unusual LREE-, Th-, Nb-, U-rich oxide grain. This grain has an LREE pattern unlike that found in other spots. It does not have the pronounced enrichment in Ce relative to La and Pr or the depletion in Nd relative to Pr and Sm.

Magnesium and Titanium Isotopic Analysis

The isotopic compositions of Mg and Ti in HIB-11 were determined by ion microprobe and are shown in Table 4. Small

TABLE 3. Major and trace element abundances in HIB-11 determined by ion microprobe (ppm unless otherwise indicated).

	1	2	3	4
MgO (%)	6.65	3.47	7.24	5.53
Al ₂ O ₃ (%)	33.4	11.5	30.9	27.4
SiO ₂ (%)	14.8	4.8	10.0	18.1
CaO (%)	21.5	37.9	25.2	23.8
Sc ₂ O ₃ (%)	9.15	1.50	6.06	5.37
TiO ₂ (%)	12.4	38.0	18.4	16.1
V ₂ O ₃ (%)	0.57	0.31	0.42	0.60
FeO (%)	0.22 ± 0.03	0.27 ± 0.03	0.21 ± 0.04	0.43 ± 0.06
Li	0.23 ± 0.06	0.36 ± 0.07	0.33 ± 0.08	0.71 ± 0.13
Be	0.84 ± 0.14	0.53 ± 0.11	1.03 ± 0.19	1.45 ± 0.24
F	187 ± 32	209 ± 35	401 ± 60	337 ± 58
Na	1042	4399	931	5508
Cl	143 ± 35	395 ± 57	211 ± 51	676 ± 102
K	62.8 ± 4.3	147 ± 7	75.1 ± 6.0	371
Cr	806	370 ± 16	554	962
Mn	59 ± 16	40 ± 5	66 ± 12	114 ± 20
Rb	92.2 ± 5.1	10.2 ± 1.6	42.6 ± 3.9	46.6 ± 4.9
Sr	86.3 ± 2.9	287	119	116
Y	2593	7044	4236	4004
Zr	3427	966	3118	2003
Nb	42.2 ± 2.9	185	101	68.0 ± 4.8
Cs	< 1.54	< 0.94	< 1	< 2.4
Ba	6.06 ± 1.19	19.3 ± 1.9	5.18 ± 1.15	38.7 ± 4.2
La	1.90 ± 0.27	12.3	2.43 ± 0.32	270
Ce	14.2 ± 1.2	154	27.3 ± 1.7	974
Pr	0.51 ± 0.29	12.5 ± 1.3	2.38 ± 0.66	131
Nd	2.84 ± 1.16	29.2 ± 3.1	4.43 ± 1.46	490
Sm	3.04 ± 0.52	23.1 ± 1.2	3.70 ± 0.57	119
Eu	1.18 ± 0.19	6.08 ± 0.36	1.44 ± 0.21	4.29 ± 0.48
Gd	23.3 ± 3.2	104 ± 6	27.0 ± 3.6	71.0 ± 9.9
Tb	19.1 ± 1.1	86.3	27.7 ± 1.4	55.5 ± 2.9
Dy	607	2156	791	1295
Ho	315	841	406	586
Er	433	911	583	734
Tm	7.44 ± 0.59	10.3 ± 0.6	9.18 ± 0.65	10.3 ± 0.9
Yb	22.8 ± 2.2	33.4 ± 2.9	31.9 ± 2.5	37.1 ± 3.8
Lu	9.13 ± 0.99	6.26 ± 1.46	13.7 ± 1.1	15.7 ± 1.6
Pb	74 ± 37	59 ± 26	< 58	401 ± 115
Th	0.66 ± 0.27	1.93 ± 0.35	< 0.26	400
U	0.89 ± 0.31	2.46 ± 0.39	0.89 ± 0.28	16.2 ± 1.8

Errors given are $\pm 1\sigma$, based on counting statistics, and are only given where they exceed 5% of the amount present; upper limits are $< 2\sigma$. Phases analyzed: (1) Fassaite (Fass) + minor spinel (Sp); (2) Perovskite (Pv) + minor Sp and Fass; (3) Fass + Sp + Pv in roughly equal proportions; (4) Fass + Sp + Pv, with more Fass than (3).

excesses of ^{26}Mg are observed, suggesting that some live ^{26}Al was present at the time of formation of HIB-11. If we assume that HIB-11 had normal isotopic composition before ^{26}Al decay, we can calculate initial $^{26}\text{Al}/^{27}\text{Al}$ ratios from the data in Table 4. The ratios, $(11.3 \pm 4.8, 8.6 \pm 6.2, 20.8 \pm 9.4) \times 10^{-5}$, are higher than the canonical early solar system $^{26}\text{Al}/^{27}\text{Al}$ ratio of 5×10^{-5} . But high inferred initial $^{26}\text{Al}/^{27}\text{Al}$ ratios are often seen in low Al/Mg phases and generally indicate partial Mg-isotopic redistribution after some or all of the ^{26}Al decayed (MacPherson *et al.*, 1995).

All Ti isotopic measurements are within 3σ analytical uncertainty of normal isotopic composition. The Ti mass fractionation, F_{Ti} , was calculated in the usual way except that it was multiplied by -1 so that enrichment in the heavy isotopes would give positive values. HIB-11 has no detectable Ti isotopic mass fractionation or ^{50}Ti nuclear anomalies (Table 4); Davis (1991) found that three

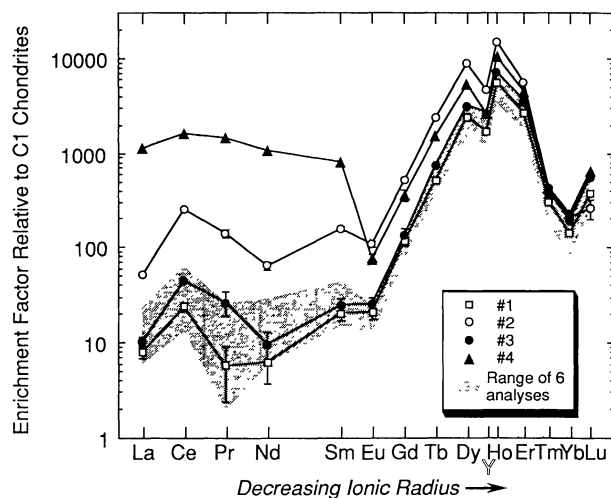


FIG. 3. Chondrite-normalized REE and Y abundances in HIB-11, determined by ion microprobe. Error bars are shown where they are larger than the symbols. Patterns, shown for the analyses given in Table 3 and numbered accordingly, exhibit similar enrichments and depletions despite differences in the fassaite:spinel:perovskite ratios of the analytical volumes. Eight analyses were collected, six of which, including the two shown, fall within the shaded area. The C1 values are from Anders and Grevesse (1989).

other ultrarefractory inclusions also contain unfractionated Ti. These results contrast sharply with those for non-ultrarefractory, hibonite-bearing inclusions from Murchison in which significant enrichments or depletions in ^{50}Ti are commonly found (e.g., Ireland, 1988). Significant Ti isotopic mass fractionation has only been reported in five hibonite-rich inclusions that have a number of isotopic and chemical properties characteristic of evaporation residues (Ireland *et al.*, 1992; Fahey *et al.*, 1994).

DISCUSSION

Volatility Fractionation of the Rare Earth Elements During Condensation

HIB-11 is the first known inclusion in which the most refractory HREE are strongly fractionated from the less refractory HREE. It has a very complex REE pattern that appears to have been influenced by several stages of high-temperature volatility fractionation. At these temperatures, Mg would be completely vaporized, but Ti would be only partially evaporated. The absence of mass fractionation among the Ti isotopes (Table 4) indicates that HIB-11

TABLE 4. Magnesium and Ti isotopic compositions of HIB-11.

Analysis #	$^{27}\text{Al}/^{24}\text{Mg}$	$\Delta^{25}\text{Mg}$ (‰)	$\delta^{26}\text{Mg}$ (‰)		
1	5.2 ± 0.2	-5.0 ± 1.5	4.2 ± 1.8		
2	3.4 ± 0.2	-1.2 ± 1.1	2.1 ± 1.5		
3	5.5 ± 0.2	-1.0 ± 2.6	8.2 ± 3.7		
	F_{Ti} (‰/amu)	$\delta^{47}\text{Ti}$ (‰)	$\delta^{49}\text{Ti}$ (‰)	$\delta^{50}\text{Ti}$ (‰)	
4	-1.7 ± 3.2	2.1 ± 3.0	6.8 ± 5.6	4.0 ± 6.6	
5	-1.9 ± 4.1	-3.3 ± 3.4	3.4 ± 6.7	10.3 ± 12.1	
6	-3.0 ± 7.3	-4.4 ± 5.6	5.6 ± 8.0	9.4 ± 17.6	
avg	-2.2 ± 3.0	-1.8 ± 2.4	6.1 ± 4.4	7.9 ± 7.4	

All spots are in fassaite + spinel ± perovskite. Uncertainties are $\pm 2\sigma$.

is not an evaporation residue and that its fractionated REE pattern was produced during condensation. In order to understand this pattern, it is first necessary to understand the relative volatilities of the REE and a few other key refractory elements by estimating their solid/gas distribution coefficients. Davis and Grossman (1979) explored in detail the condensation behavior of REE. In most of their calculations, they assumed ideal solid solution in likely host phases (perovskite and hibonite) because activity coefficients for solid solution of REE in these phases were not available. That situation persists today; however, measurements of mineral/melt partition coefficients clearly show that REE solid solution in hibonite and perovskite is not ideal (*e.g.*, Kennedy *et al.*, 1994). We used activity coefficients for hibonite estimated by MacPherson and Davis (1994). They assumed that the melt used in the hibonite/melt partitioning experiment of Kennedy *et al.* (1994) has the same activity coefficient for all REE. MacPherson and Davis used the activity coefficient of 0.02 inferred by Hinton *et al.* (1988) for La in hibonite and calculated the remaining activity coefficients for REE and Y in hibonite, assuming that activity coefficients are proportional to melt/hibonite partition coefficients. The latter data were obtained from Kennedy *et al.* (1994) by making a parabolic fit to the hibonite/melt partition coefficient vs. ionic radius relationship. Activity coefficients for perovskite were estimated from the perovskite/melt partitioning data of Kennedy *et al.* (1994) in the same way, assuming that activity coefficients in the melt were the same as in the hibonite/melt experiment.

Additional potential host phases for REE during high-temperature condensation are baddeleyite and a mixed Zr-, Sc-, Ti-, Y-oxide. There are no measurements of baddeleyite/melt partition coefficients, but it seems likely that baddeleyite would favor HREE because Zr^{+4} has a small ionic radius. Also, it is the only element for which REE can substitute. The REE also substitute for Zr^{+4} in zircon, which is known to strongly favor HREE over LREE. Lacking any further information, we have assumed that zircon and baddeleyite have the same activity coefficients for solid solution of REE and have calculated activity coefficients from the zircon/melt partition coefficients of Hinton and Upton (1991) by assuming that all melts from which zircon/melt partition coefficients have been calculated have the same REE activity coefficients as melts used in hibonite and perovskite crystal/melt partitioning experiments. Hinton *et al.* (1988) were able to analyze tiny inclusions of REE-rich phases in corundum in the Murchison corundum-hibonite inclusion BB-5. They found one phase with a low Gd/Lu ratio that contained ~65% ZrO_2 , 13% TiO_2 , 7% Sc_2O_3 , 7% CaO , 6% Y_2O_3 , and 2% HREE oxides. These data suggest that a mixed Zr-, Sc-, Ti-, Y-oxide favors HREE, but it is not possible to make estimates of activity coefficients for this phase from the data of Hinton *et al.* Activity coefficients for solid solution of REE and Y in hibonite, perovskite, and zircon inferred here are given in Table 5.

MacPherson and Davis (1994) pointed out that relative gas/solid distribution coefficients for REE are not very sensitive to temperature. Using the activity coefficients in Table 5, we have calculated relative solid/gas distribution coefficients for REE and Y at 1741 K, which is 1.8° below the condensation temperature of hibonite at $P_{tot} = 10^{-3}$ atm (Yoneda and Grossman, 1995), and the results are shown in Fig. 4. Thermodynamic data used for REE and Y are the same as those used by MacPherson and Davis (1994).

There are a number of important features of the REE pattern of HIB-11 that can be understood using this plot. Ytterbium is much more volatile than the other HREE, and Tm is significantly more

TABLE 5. Activity coefficients for solid solution of REE and Y in hibonite, perovskite, and baddeleyite, inferred from mineral/melt partitioning experiments.

	hibonite	perovskite	baddeleyite
Y	0.404	0.0445	0.00302
La	0.0200	0.0111	13.9
Ce	0.0219	0.0100	5.04
Pr	0.0259	0.00971	1.82
Nd	0.0330	0.0102	0.659
Sm	0.0604	0.0132	0.109
Eu	0.0843	0.0159	0.0503
Gd	0.123	0.0199	0.0231
Tb	0.187	0.0262	0.0106
Dy	0.298	0.0359	0.00487
Ho	0.474	0.0499	0.00238
Er	0.751	0.0697	0.00123
Tm	1.17	0.0970	0.000676
Yb	1.79	0.134	0.000395
Lu	2.65	0.181	0.000245

volatile than Er and Lu. Of the refractory (all except Tm and Yb) HREE, volatility decreases in the order Gd, Tb, Dy, Ho, Er, and Lu; Y is intermediate in volatility between Ho and Er. Considering just the refractory HREE in HIB-11, enrichment factors increase from Gd to Ho but drop from Ho to Er and Lu (Fig. 3). It thus seems likely that a fraction of the most refractory HREE, most of the Er and Lu, and some of the Y were removed in an early condensate. The Ho/Lu ratio of bulk HIB-11 is 20× C1, implying that the first fractionation episode was capable of fractionating the Lu/Ho ratio by at least this much. Examination of Fig. 4 shows that, of the examples shown, only baddeleyite (which favors HREE over LREE) or a phase with uniform REE activity coefficients is likely to produce this degree of Lu/Ho fractionation. A mixed Zr-, Sc-, Ti-, Y-oxide is also a possibility, as it also favors HREE over LREE.

In contrast, as can be seen from Fig. 4, D_{Lu}/D_{Ho} ratios in both perovskite and hibonite are <20, which is too low to fractionate these elements from each other by the observed factor of 20 unless fractional condensation occurred. Analogous to fractional crystallization from a liquid, this process can yield a more highly fractionated residual vapor than that assumed above if an element with a high condensation temperature (*e.g.*, Lu) is concentrated relative to one with a lower condensation temperature (*e.g.*, Ho) in the solid phase, and the condensates fail to reequilibrate with the gas. A necessary condition for this to happen is that condensation rates of the solids have to be faster than diffusion rates of the elements of interest in those solids. In order to determine the importance of fractional condensation, we have compared the time scales for diffusion over a distance of 1 μm with those for condensation of a layer 1 μm thick for hibonite and for perovskite. The rate of growth of a condensate phase is limited by the rate of impingement of atoms or molecules in the gas on the surface of the growing crystal. The impingement rate for each constituent element of a condensate phase can be calculated from the temperature, pressure, and composition of the gas using the kinetic theory of gases. The impingement rate gives the maximum condensation rate; if the sticking coefficient is <1, as is likely, condensation will be slower. The time scale for diffusion is calculated from $t = l^2/D$, where t is time, l is distance, and D is the diffusion coefficient.

For the first condensate, the concentrations of the most refractory elements will be quite high. The Lu content of first-

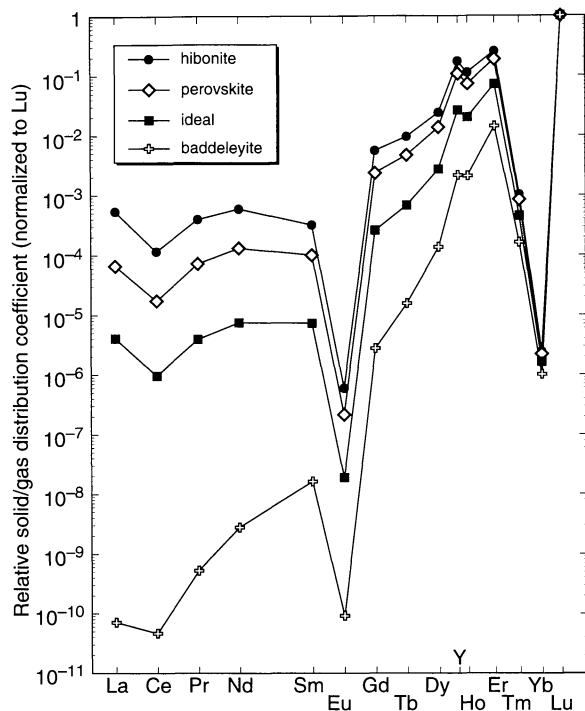


FIG. 4. Solid/gas distribution coefficients for REE and Y relative to that for Lu, for various mineral phases in a gas of solar composition at 1741 K. The curve labelled "ideal" is for ideal solution into a solid that has uniform REE activity coefficients and, therefore, reflects only the effects of volatility differences.

formed hibonite at 1742 K, with only 0.01% of total Ca condensed in it, will be ~ 1500 ppm. From the abundance of Lu in the nebular gas, we estimate that it requires at least 23 days to condense a $1 \mu\text{m}$ thick layer of hibonite with 1500 ppm Lu. Diffusion rates have been measured for Al in Al_2O_3 (Paladino and Kingery, 1962); if diffusion coefficients for REE in hibonite are similar, they are likely to be on the order of $10^{-13} \text{ cm}^2 \text{ s}^{-1}$ at 1742 K, which is the equilibrium condensation temperature of hibonite. The time scale for diffusion over a distance of $1 \mu\text{m}$ using this diffusion coefficient is ~ 1 day, so fractional condensation does not seem plausible for hibonite, even with a sticking coefficient of 1. Of course, if diffusion rates for REE in hibonite are determined to be substantially slower, it will be necessary to reconsider the effects of fractional condensation. But based on the data presently available, hibonite condensation could not have caused the Lu/Ho fractionation preserved in HIB-11.

The idea that perovskite is the likely host phase for initial condensation of REE dates back to the work of Grossman (1973). At that time, the condensation temperature of hibonite was not calculable because no thermodynamic data were available, and ZrO_2 was not considered at that time. We now know that perovskite first condenses from a gas of solar composition at 10^{-3} atm total pressure at 1688 K (Yoneda and Grossman, 1995), which is well below the initial condensation temperature of hibonite (1743 K) (Yoneda and Grossman, 1995). If perovskite were the condensate phase responsible for the high temperature gas-solid fractionation event, the condensation of hibonite, and probably of ZrO_2 , must have been suppressed for some reason. The Lu content of first-formed perovskite, with only 0.01% of total Ca in it, will be ~ 8000 ppm, and it requires at least 234 days to condense a $1 \mu\text{m}$ thick layer of

perovskite with this much Lu. We know little about diffusion rates in perovskite, but the diffusion coefficients for REE in perovskite would have to be very low, on the order of $10^{-15} \text{ cm}^2 \text{ s}^{-1}$ – $10^{-16} \text{ cm}^2 \text{ s}^{-1}$, in order for diffusion in perovskite to be slower than condensation. Fractional condensation thus seems unlikely for perovskite, and it is also unlikely that perovskite was the host phase because its condensation temperature is substantially lower than those of other possible host phases.

The sharp increase in enrichment factor of HREE from Gd to Ho in HIB-11 suggests that the REE remaining in the gas after removal of Er, Lu, and Zr did not completely condense into the HIB-11 precursors. The Ho/Gd ratio of HIB-11 is $42 \times \text{C1}$, so the second condensation step must be capable of fractionating this ratio by at least this much. The maximum fractionations that can be produced by perovskite or hibonite condensation are 31 and 20, respectively, so it seems likely that this second condensation episode also involved baddeleyite, or a mixed Zr-, Sc-, Ti-, Y-oxide, or a phase with uniform REE activity coefficients and occurred at a temperature greater than that of hibonite condensation.

The LREE pattern of HIB-11 has some structure to it that also appears to be volatility-related. Hinton *et al.* (1988) showed that the LREE pattern of an unusual corundum-hibonite inclusion, GR-1, could be explained by incomplete condensation of REE from a gas that initially contained the REE in C1 chondritic relative proportions. Incomplete condensation of LREE produces a pattern in the condensate with similar relative enrichments of La, Pr, and Sm, a depletion in Ce relative to La and Pr, and a small enrichment in Nd relative to Pr and Sm, as calculated in Fig. 4 for hibonite, perovskite, or a phase with uniform activity coefficients. HIB-11 shows the opposite trend. It is enriched in the most volatile LREE, Ce, and slightly depleted in the most refractory one, Nd. Such LREE patterns have been observed previously in so-called "modified group II" REE patterns and, in these inclusions, are probably due to prior, partial condensation, and removal of the most refractory LREE along with a major fraction of the HREE. In HIB-11, however, this fractionation episode is probably independent of the ones responsible for the depletion of Er and Lu relative to other HREE and of Gd, Tb, and Dy relative to Ho. This is because the HREE fractionation pattern was formed by incomplete condensation, which is a process that would have created the opposite of the fractionation pattern seen among the LREE. The LREE abundances in HIB-11 probably reflect complete condensation from a residual gas that had undergone prior, partial condensation and removal of LREE (*i.e.*, a Nd-rich, Ce-poor component). The Ce-rich condensates were then mixed with the HREE-rich HIB-11 precursor grains.

Finally, all condensation calculations show that Eu and Yb are much more volatile than the other REE, yet Eu and Yb in HIB-11 are only slightly depleted relative to neighboring REE. This is another aspect in which HIB-11 resembles the "modified group II" inclusions. The final condensation episode in which the LREE condensed into the HIB-11 precursors may have occurred at a lower temperature than is normal for a group II inclusion, so that Eu and Yb were able to condense. This lower-temperature component may have been introduced into the precursors to HIB-11 at the same time as the less refractory major elements, Si and Mg.

Formation of HIB-11

We can understand the chondrite-normalized REE pattern of HIB-11 in terms of a series of condensation events, but whether the phases observed in the inclusion are condensates is a separate question, and we address it here.

It is highly unlikely that the phases observed in HIB-11 are primary condensates. As explained above, the chondrite-normalized REE pattern of HIB-11 reflects several events, one of which involves partial condensation of HREE into HIB-11 precursors. These events are restricted to temperatures greater than or equal to that of hibonite stability, 1743 K (Yoneda and Grossman, 1995), because within just a few K of this temperature all REE except Eu and Yb are completely condensed. Perovskite condenses at 1688 K (Yoneda and Grossman, 1995), which is well after hibonite condenses. The equilibrium condensation temperature for Sc-fassaite from a solar gas is not known, but for Ti-fassaite it is 1449 K (Yoneda and Grossman, 1995), almost 300 K below that of hibonite. Thus, both perovskite and fassaite have condensation temperatures below that of hibonite; yet, in HIB-11, they have a HREE fractionation pattern calculated for a temperature above the condensation temperature of hibonite and for phases that are not observed in the inclusion. This is inconsistent with interpretation of HIB-11 as a primary condensate.

An alternative explanation is that HIB-11 had solid condensate precursors that were melted, forming a liquid from which spinel, fassaite, and perovskite crystallized. The crystallization sequence of a liquid with the bulk composition of HIB-11 has not been investigated experimentally, but if normalized to 100% CaO + MgO + Al₂O₃ + SiO₂ + TiO₂, the composition can be projected from spinel onto the CaMgSi₂O₆(Di)-CaTiAl₂O₆(T₄P)-CaAl₂SiO₆(CaTs) plane, for which data are available (Onuma and Kimura, 1978). The HIB-11 composition plots at 30.6% Di, 64.2% T₄P, and 5.2% CaTs in the spinel field of the liquidus diagram. Compositions of Type B CAIs also project into the spinel field (Onuma and Kimura, 1978) but do not plot as close to the Di-T₄P join as HIB-11. The phase equilibria indicate that spinel should have crystallized first in HIB-11, to be joined first by perovskite, then by melilite (for a brief interval), anorthite, and finally Ti-pyroxene. Melilite and anorthite are absent from HIB-11, but the other three phases predicted to crystallize (spinel, perovskite, and Ti-pyroxene) are present in a texture consistent with cocrystallization of spinel and fassaite. We, therefore, conclude that the assemblage observed in HIB-11 is consistent with crystallization of the inclusion from a liquid, assuming that the ~5 wt% Sc₂O₃ present stabilized pyroxene relative to melilite and anorthite, thereby causing Sc-fassaite to crystallize instead of the latter phases.

The nonequilibrium distribution of trace elements provides evidence for rapid cooling. Although we analyzed no monomineralic spots with the ion probe, analysis #1 in Table 3 is mostly fassaite with minor amounts of spinel, and the latter has negligible REE contents. Analysis #4 has a high fassaite component as well, but it contains both spinel and perovskite and has anomalous LREE abundances. We, therefore, take analysis #1 to be representative of the fassaite REE pattern. Analysis spot 2 is strongly dominated by perovskite, and this pattern can be taken as representative of the perovskite REE pattern. If these phases cocrystallized from a melt at equilibrium, the ratios of their trace element abundances should equal the ratios of their crystal/liquid distribution coefficients (Ds). On a plot of D_{pv}/D_{fass} vs. $Conc_{pv}/Conc_{fass}$ (analysis #2/analysis #1) for the REE and Y (Fig. 5), we observe a 1:1 correlation for some, but not all, of the elements analyzed. In general, the greater the ionic radius, the greater the deviation from the 1:1 reference line. Davis *et al.* (1992) noted an analogous relationship among analyses of igneous melilite in the mantles of Type B1 CAIs. They found that abundances of larger cations of a given valence deviated further

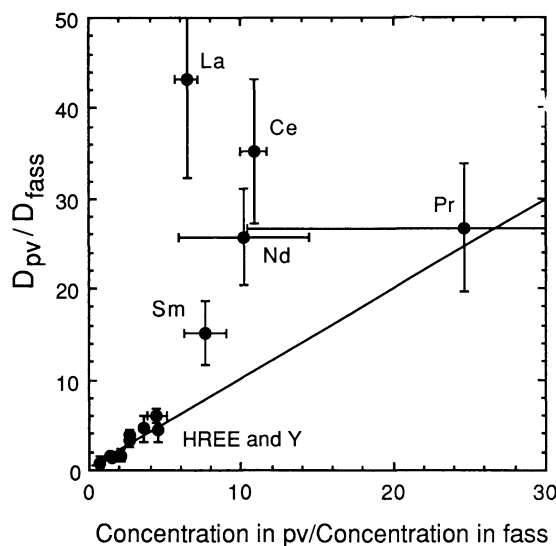


FIG. 5. Comparison of the ratios of Ds for perovskite (Kennedy *et al.*, 1994) and fassaite ("early" Ds from Simon *et al.*, 1991) to the ratios of observed abundances in those phases in HIB-11. In general, the greater the ionic radius, the greater the deviation from the 1:1 reference line, with observed abundances of LREE lower than values expected from equilibrium Ds.

from predicted abundances than did those of smaller cations of the same valence. Davis *et al.* (1992) attributed these systematics to boundary layer formation in the melt, with slow diffusion relative to crystal growth causing build-ups of incompatible elements in the liquid. They further reasoned that larger cations, such as LREE, would have slower diffusion rates and greater build-ups in the liquid; hence, there would be larger deviations from predicted abundances than the smaller cations, such as HREE. Boundary layer formation could also account for the deviations of LREE abundance ratios from those predicted from ratios of equilibrium Ds. Kennedy *et al.* (1994) reported Ds for LREE in perovskite of ~9–14, whereas those for fassaite are ~0.2–0.7 (Simon *et al.*, 1991). Boundary layer formation in HIB-11 would, therefore, result in LREE concentrations in perovskite that are lower, and concentrations in fassaite that are higher, than would be predicted from equilibrium partitioning. This would lead to lower $Conc_{pv}/Conc_{fass}$ ratios for LREE than predicted from ratios of equilibrium Ds, as is observed (Fig. 5). For HREE, with presumably faster diffusion rates than LREE in the liquid and with Ds in both perovskite and fassaite closer to 1 than those for LREE, boundary layer effects would be minimal, in agreement with our observation of only slight to no deviation from the predicted abundance ratios for HREE. Our observations can, therefore, be considered consistent with crystallization of HIB-11 from a liquid, with the nonequilibrium distribution of slowly diffusing trace elements and fine grain-size of the constituent minerals indicating formation of HIB-11 by rapid crystallization. In addition, the rounded shape of the inclusion and the rounded cavity that is probably a vesicle are also consistent with solidification of a once-molten droplet.

This makes it difficult to account for the unusual habit of the lathlike spinel crystals in HIB-11, however, since crystals such as these have not been produced in crystallization experiments on liquids with bulk compositions like those of CAIs, even in runs cooled at 1000 °C h⁻¹ (Stolper and Paque, 1986). In the few inclusions where lathlike spinel has been observed, it has been

inferred to have replaced hibonite (MacPherson *et al.*, 1984; MacPherson and Davis, 1994), and, indeed, equilibrium condensation calculations show that condensate hibonite should react with the nebular gas to form spinel (Yoneda and Grossman, 1995). The elongated spinel grains found in HIB-11 may have also formed by replacement of hibonite and then were mixed with the HIB-11 precursors prior to melting. Some of the spinel laths survived the melting event, while the anhedral spinel that is intergrown with pyroxene crystallized from the melt.

It has been shown that Sc_2O_3 is compatible in fassaite and Y_2O_3 is not (Simon *et al.*, 1991), so Y_2O_3 should be negatively correlated with Sc_2O_3 in fassaite crystallized from a melt. Initial fassaite should be relatively high in Sc and low in Y, and later-formed fassaite should have lower Sc and higher Y contents. On a plot of Y_2O_3 vs. Sc_2O_3 in HIB-11 fassaite (Fig. 2d), all analyses appear to scatter, but among grains with >10 wt% Sc_2O_3 (solid symbols), there is a good negative correlation between Y_2O_3 and Sc_2O_3 , as expected from fractional crystallization. The lower Y_2O_3 contents of several of the fassaite points with lower Sc_2O_3 contents may represent late fassaite that crystallized after much of the perovskite. Yttrium is quite compatible in perovskite (Simon *et al.*, 1994a), so perovskite crystallization will tend to deplete a melt in Y_2O_3 . These data are, therefore, also consistent with crystallization of the inclusion from a liquid. A melt droplet of this size should have equilibrated with the nebular gas, so the relatively low $\text{Ti}^{3+}/\text{Ti}^{\text{tot}}$ ratios in HIB-11 fassaite, compared to those of fassaite in Type B inclusions, may reflect melting under relatively oxidizing conditions. Interpretation of $\text{Ti}^{3+}/\text{Ti}^{\text{tot}}$ ratios is not so straightforward, however, because the $\text{Ti}^{3+}/\text{Ti}^{\text{tot}}$ ratio of fassaite in equilibrium with a gas of solar composition varies irregularly with temperature (Yoneda and Grossman, 1995). Furthermore, liquid bulk composition, reactions between phases, and the relative stabilities of the other fassaite components (Di, CaTs) all affect the $\text{Ti}^{3+}/\text{Ti}^{\text{tot}}$ ratio of fassaite in addition to f_{O_2} .

SUMMARY AND CONCLUSIONS

The refractory inclusion HIB-11 has a unique texture and bulk composition. It consists of Sc-fassaite, spinel, and perovskite, and is slightly less refractory than previously described ultrarefractory inclusions. As in the latter, HREE are strongly enriched relative to LREE in HIB-11; but, in this inclusion, the chondrite-normalized abundances of Lu and Er, the most refractory REE, are lower than that of Ho, the next most refractory REE. In other ultrarefractory inclusions, Lu is the REE with the greatest enrichment factor. An absence of significant fractionation of the Ti isotopes in HIB-11 indicates that the REE pattern was established during condensation, not evaporation. Several condensation stages are required to produce the complex REE pattern. The first step is depletion of Lu and Er relative to the other REE by condensation from the source gas. The second step is condensation of the HIB-11 precursors from the residual gas, at a high enough temperature that the HREE only partially condensed, yielding the increase in enrichment factors from Gd through Ho observed in HIB-11. Calculations show that for both stages, neither hibonite nor perovskite condensation could produce the observed degrees of fractionation and that condensation into baddeleyite, a mixed Zr-, Sc-, Ti-, Y-oxide, or a phase with uniform activity coefficients is much more likely to have produced the observed fractionations. These condensates were later mixed with a fractionated LREE carrier (enriched in Ce and depleted in Nd relative to Sm) and then melted and quickly cooled.

The chondrite-normalized REE pattern of HIB-11 shows that fractionation occurs even among the most refractory HREE, suggesting that refractory inclusions with other strongly fractionated REE patterns may yet be discovered. A more complete suite of such inclusions would provide a valuable record of the early stages of condensation of the solar nebula.

Acknowledgments—We wish to thank A. Hsu for performing the disaggregation, P. Sylvester for performing the density separation, and S. Yoneda for providing condensation calculations and helpful discussions. Reviews by G. MacPherson and W. Boynton led to improvements in the text. This work was supported by the National Aeronautics and Space Administration through grants NAG 9-54 and NAGW-3340 (LG), NAGW-3384 (AMD) and NAGW-3345 (to R. N. Clayton).

Editorial handling: S. R. Taylor

REFERENCES

- ANDERS E. AND GREVESSE N. (1989) Abundances of the elements: Meteoritic and solar. *Geochim. Cosmochim. Acta* **53**, 197–214.
- BECKETT J. R. (1986) The origin of calcium-, aluminum-rich inclusions from carbonaceous chondrites: An experimental study. Ph.D. thesis, University of Chicago. 373 pp.
- BOYNTON W. V. (1975) Fractionation in the solar nebula: Condensation of yttrium and the rare earth elements. *Geochim. Cosmochim. Acta* **39**, 569–584.
- BOYNTON W. V., FRAZIER R. M. AND MACDOUGALL J. D. (1980) Identification of an ultra-refractory component in the Murchison meteorite (abstract). *Lunar Planet. Sci.* **11**, 103–105.
- DAVIS A. M. (1984) A scandalously refractory inclusion in Ormans (abstract). *Meteoritics* **19**, 214.
- DAVIS A. M. (1991) Ultrarefractory inclusions and the nature of the group II REE fractionation (abstract). *Meteoritics* **26**, 330.
- DAVIS A. M. AND GROSSMAN L. (1979) Condensation and fractionation of rare earths in the solar nebula. *Geochim. Cosmochim. Acta* **43**, 1611–1632.
- DAVIS A. M., MACPHERSON G. J., CLAYTON R. N., MAYEDA T. K., SYLVESTER P. J., GROSSMAN L., HINTON R. W. AND LAUGHLIN J. R. (1991) Melt solidification and late-stage evaporation of a FUN inclusion from the Vigarano C3V chondrite. *Geochim. Cosmochim. Acta* **55**, 621–637.
- DAVIS A. M., SIMON S. B. AND GROSSMAN L. (1992) Melilite composition trends during crystallization of Allende Type B1 refractory inclusion melts (abstract). *Lunar Planet. Sci.* **23**, 281–282.
- EKAMBARAM V., KAWABE I., TANAKA T., DAVIS A. M. AND GROSSMAN L. (1984a) Chemical compositions of refractory inclusions in the Murchison C2 chondrite. *Geochim. Cosmochim. Acta* **48**, 2089–2105.
- EKAMBARAM V., SLUK S. M., GROSSMAN L. AND DAVIS A. M. (1984b) Trace elements in high-temperature inclusions from Murchison (abstract). *Meteoritics* **19**, 222–223.
- EL GORESY A., PALME H., YABUKI H., NAGEL K., HERRWERTH I. AND RAMDOHR P. (1984) A calcium-aluminum-rich inclusion from the Essebi (CM2) chondrite: Evidence for captured spinel-hibonite spherules and for an ultra-refractory rimming sequence. *Geochim. Cosmochim. Acta* **48**, 2283–2298.
- FAHEY A. J., ZINNER E., KURAT G. AND KRACHER A. (1994) Hibonite-hercynite inclusion HH-1 from the Lancé (CO3) meteorite: The history of an ultrarefractory CAI. *Geochim. Cosmochim. Acta* **58**, 4779–4793.
- GROSSMAN L. (1973) Refractory trace elements in Ca-Al-rich inclusions in the Allende meteorite. *Geochim. Cosmochim. Acta* **37**, 1119–1140.
- HINTON R. W. AND UPTON B. G. J. (1991) The chemistry of zircon: Variations within and between large crystals from syenite and alkali basalt xenoliths. *Geochim. Cosmochim. Acta* **55**, 3287–3302.
- HINTON R. W., DAVIS A. M., SCATENA-WACHEL D. E., GROSSMAN L. AND DRAUS R. J. (1988) A chemical and isotopic study of hibonite-rich refractory inclusions in primitive meteorites. *Geochim. Cosmochim. Acta* **52**, 2573–2598.
- IRELAND T. R. (1988) Correlated morphological, chemical, and isotopic characteristics of hibonites from the Murchison carbonaceous chondrite. *Geochim. Cosmochim. Acta* **52**, 2827–2839.
- IRELAND T. R., ZINNER E. K., FAHEY A. J. AND ESAT T. M. (1992) Evidence for distillation in the formation of HAL and related hibonite inclusions. *Geochim. Cosmochim. Acta* **56**, 2503–2520.
- KENNEDY A. K., LOFGREN G. E. AND WASSERBURG G. J. (1994) Trace-element partition coefficients for perovskite and hibonite in meteorite compositions. *Chem. Geol.* **117**, 379–390.

- MACDOUGALL J. D. (1981) Refractory spherules in the Murchison meteorite: Are they chondrules? *Geophys. Res. Lett.* **8**, 966–969.
- MACPHERSON G. J. AND DAVIS A. M. (1993) A petrologic and ion microprobe study of a Vigarano Type B refractory inclusion: Evolution by multiple stages of alteration and melting. *Geochim. Cosmochim. Acta* **57**, 231–243.
- MACPHERSON G. J. AND DAVIS A. M. (1994) Refractory inclusions in the prototypical CM chondrite, Mighei. *Geochim. Cosmochim. Acta* **58**, 5599–5625.
- MACPHERSON G. J. AND GROSSMAN L. (1984) "Fluffy" Type A Ca-, Al-rich inclusions in the Allende meteorite. *Geochim. Cosmochim. Acta* **48**, 29–46.
- MACPHERSON G. J., BAR-MATTHEWS M., TANAKA T., OLSEN E. AND GROSSMAN L. (1980) Refractory inclusions in Murchison: Recovery and mineralogical description (abstract). *Lunar Planet. Sci.* **11**, 660–662.
- MACPHERSON G. J., BAR-MATTHEWS M., TANAKA T., OLSEN E. AND GROSSMAN L. (1983) Refractory inclusions in the Murchison meteorite. *Geochim. Cosmochim. Acta* **47**, 823–839.
- MACPHERSON G. J., GROSSMAN L., HASHIMOTO A., BAR-MATTHEWS M. AND TANAKA T. (1984) Petrographic studies of refractory inclusions from the Murchison meteorite. *Proc. Lunar Planet. Sci. Conf.* **15th**, *J. Geophys. Res. (suppl.)* **89**, C299–C312.
- MACPHERSON G. J., DAVIS A. M. AND ZINNER E. K. (1995) The distribution of aluminum-26 in the early Solar System—A reappraisal. *Meteoritics* **30**, 365–386.
- MASON B. AND MARTIN P. M. (1977) Geochemical differences among components of the Allende meteorite. *Smithson. Contrib. Earth Sci.* **19**, 84–95.
- NOONAN A. F., NELEN J., FREDRIKSSON K. AND NEWBURY D. (1977) Zr-Y oxides and high-alkali glass in an ameboid inclusion from Ornans (abstract). *Meteoritics* **12**, 332–335.
- ONUMA K. AND KIMURA M. (1978) Study of the system $\text{CaMgSi}_2\text{O}_6$ - $\text{CaFe}^{3+}\text{AlSiO}_6$ - $\text{CaTiAl}_2\text{O}_6$: II. The join $\text{CaMgSi}_2\text{O}_6$ - $\text{CaAl}_2\text{SiO}_6$ - $\text{CaTiAl}_2\text{O}_6$ and its bearing on Ca-Al-rich inclusions in carbonaceous chondrite. *J. Fac. Sci., Hokkaido Univ. Ser. IV* **18**, 215–236.
- PALADINO A. E. AND KINGERY W. D. (1962) Aluminum ion diffusion in aluminum oxide. *J. Chem. Phys.* **37**, 957–962.
- PALME H., WLOTZKA F., NAGEL K. AND EL GORESY A. (1982) An ultra-refractory inclusion from the Ornans carbonaceous chondrite. *Earth Planet. Sci. Lett.* **61**, 1–12.
- POUCHOU J. L. AND PICOIR F. (1984) A new model for quantitative X-ray microanalysis. Part I: Application to the analysis of homogeneous samples. *Rech. Aerosp.* **1984-3**, 13–38.
- SIMON S. B., GROSSMAN L. AND DAVIS A. M. (1991) Fassaite composition trends during crystallization of Allende Type B refractory inclusion melts. *Geochim. Cosmochim. Acta* **55**, 2635–2655.
- SIMON S. B., GROSSMAN L. AND HSU A. (1993) Petrography and origin of refractory inclusions from the Murray and Murchison C2 chondrites (abstract). *Lunar Planet. Sci.* **24**, 1309–1310.
- SIMON S. B., KUEHNER S. M., DAVIS A. M., GROSSMAN L., JOHNSON M. L. AND BURNETT D. S. (1994a) Experimental studies of trace element partitioning in Ca, Al-rich compositions: Anorthite and perovskite. *Geochim. Cosmochim. Acta* **58**, 1507–1523.
- SIMON S. B., YONEDA S., GROSSMAN L. AND DAVIS A. M. (1994b) A CaAl_4O_7 -bearing refractory spherule from Murchison: Evidence for very high-temperature melting in the solar nebula. *Geochim. Cosmochim. Acta* **58**, 1937–1949.
- STOLPER E. AND PAQUE J. M. (1986) Crystallization sequences of Ca-Al-rich inclusions from Allende: The effects of cooling rate and maximum temperature. *Geochim. Cosmochim. Acta* **50**, 1785–1806.
- SYLVESTER P. J., SIMON S. B. AND GROSSMAN L. (1993) Refractory inclusions from the Leoville, Efremovka, and Vigarano C3V chondrites: Major element differences between Types A and B, and extraordinary refractory siderophile element compositions. *Geochim. Cosmochim. Acta* **57**, 3763–3784.
- YONEDA S. AND GROSSMAN L. (1995) Condensation of $\text{CaO-MgO-Al}_2\text{O}_3$ - SiO_2 liquids from cosmic gases. *Geochim. Cosmochim. Acta* **59**, 3413–3444.